33RD CONGRESS
OF THE INTERNATIONAL COUNCIL
OF THE AERONAUTICAL SCIENCES
STOCKHOLM, SWEDEN, 4-9 SEPTEMBER, 2022
ICAS 2022 SWEDEN

OPTIMIZATION STUDY ON THE FLOW SEPARATION CONTROL USING A SAWTOOTH PLASMA ACTUATOR

Longjun Wang[1,2], Chi Wai Wong[2#] & Yu Zhou[2]

[1] Aircraft and Propulsion Laboratory, Ningbo Institute of Technology, Beihang University, Ningbo, 315832, China
[2] Center for Turbulence Control, Harbin Institute of Technology, Shenzhen 518055, China
Corresponding author, Email: cwwong@hit.edu.cn

Abstract

This experimental study aims to improve the flow separation control performance of sawtooth plasma actuator at a Reynolds number range of 0.77 × 10^5 to 3.0 × 10^5 by making the induced flow of plasma actuator opposite to the coming flow. A parametric study on the non-dimensional burst frequency F^+ (= $f_b c/U_\infty$, where f_b, c and U_∞ are the burst frequency, airfoil chord length and the free-stream velocity, respectively) and duty cycle (DC) is conducted at a post-stalled angle-of-attack α = 19°. The optimal combinations of F^+ and DC corresponding to the maximum increase of time-averaged lift coefficient C_L vary with Reynolds number. The optimum F^+ and DC increase with Reynolds number. The interaction between the induced flow by sawtooth plasma actuator and the coming flow results in the formation of the large-scale vortex aligned to the tip of the sawtooth or the small-scale vortex aligned to the trough of the sawtooth. As these vortices advect from the leading-edge to the trailing-edge of the airfoil, causing the rise in the suction pressure and further the increase of C_L.

Keywords: flow control, plasma actuator, unsteady actuation, lift enhancement, stall delay

1. Introduction

The multifunctional unmanned aerial vehicles (UAVs) and micro-aerial vehicles (MAVs) are ubiquitous in military and civilian markets. These remote-control or autonomous versatile flying vehicles are used for surveillance, early-warning, communication and mapping. Due to the small length scale and low flying velocity of these vehicles, the effective Reynolds number is in the order of $O(10^4$ - $10^6)$, which is the so-called low Reynolds number [1]. These vehicles may experience the flow separation in gust and the resultant lift drop. The scheduled missions must be abandoned due to the presence of flow separation and the deterioration of the aerodynamic performance. Active control of separated flow over an airfoil could improve its aerodynamic performance.

Dielectric barrier discharge (DBD) plasma actuator remains to be one of the most important active techniques of separation control and has gained widespread attention during the past two decades due to its unique features, such as rapid response, simple structures, high bandwidth modulation of actuation and no moving parts. Many researchers have applied the DBD plasma actuator on airfoil at low to moderate Reynolds number (*Re*), and their investigations have demonstrated significant improvement in the aerodynamic performance of airfoil. For instance, Post & Corke [2] applied a DBD plasma actuator on a NACA 663-018 airfoil at Re = 3.33 × 10^5 and delayed the airfoil stall angle of attack α_{stall} by 8°. Patel *et al*. [3] deployed a DBD plasma actuator on a NACA 0015 airfoil at Re = 7.5 × 10^5 and found a 10 - 15% increase in the time-averaged lift coefficient C_L. More importantly, the efficacy of the DBD plasma actuator has been verified at much higher Reynolds number upto Re = 2.5 × 10^6 [4]. Wang *et al*. [5] and Konstantinidis [6] have performed an excellent compendium of recent developments on DBD plasma flow control.

Several methods have been considered to increase the plasma region and the airflow velocity generated by a DBD plasma actuator, for instance, the electrode gap [7], length of the grounded electrode [8], electrode arrangement [9], and electrode shape [10,11]. Evidently, interest in the development of plasma actuators is growing rapidly; however, the improvements in momentum or velocity resulting from these methods are still limited. It remains important to develop a new technique or actuator configuration for significant improvement of control performance. In view of the recent development of DBD plasma actuators, we have developed a novel DBD plasma actuator based on two sawtooth electrodes (namely, sawtooth plasma actuator), which generated a streamwise jet and counter-rotating vortices at the tip and in the trough region of the sawtooth electrode, respectively, for flow separation control [12 - 14]. It has been found that under the "steady-mode" plasma control the α_{stall} of NACA0015 airfoil was delayed by 5° and the maximum lift coefficient C_{Lmax} was increased by 9% at Re = 0.77 × 10^5 [14]. Under the burst modulation, where the actuator was cycled on and off with a specific period, the C_{Lmax} was increased by 27.5% and the αstall was delayed by 3° [15,16]. Indeed, under the same power consumption, this sawtooth plasma actuator was found to achieve an α_{stall} of 18° and a C_{Lmax} of 0.952, which are larger than 16° and 0.892, respectively, achieved by the "traditional" DBD plasma actuator with straight-edged electrodes [14].

Zhang *et al*. [17] investigated a so-called symmetrical DBD plasma actuator, consisting a pair of narrow and wide "linear-shaped" and spanwise-oriented electrodes, on a NACA 0015 airfoil as *Re* in the range of 1.18 × 10^5 to 5.59 × 10^5. This actuator may generate uniform plasma discharge in both upstream and downstream directions. They indicated that the upstream jet induced by the symmetrical DBD plasma actuator may interact with the boundary layer and form a vortex rolling over the upper surface of the airfoil, promoting momentum exchange between low- and high-speed flow regions. Considering that the upstream-directed jet induced by their actuator was beneficial to flow separation control, one naturally wonders whether our new sawtooth plasma actuator in asymmetric configuration that generates upstream-directed and spanwise periodic discharge, namely, the upstream-directed flows, is effective for airfoil aerodynamic improvement. The objective of the present work is twofold. First, the aerodynamic effect of the airfoil with the new sawtooth plasma actuator configuration under the steady-mode and burst-modulated operation is investigated at a range of *Re*, from 0.77 × 10^5 to 3.0 × 10^5. Second, we try to gain a rudimentary understanding of the underlying flow mechanisms responsible for the aerodynamic improvement through careful examination of the smoke-wire flow visualization images with and without plasma control.

2. Experimental Setup

2.1 Wind Tunnel

Experiments are conducted in a closed-loop wind tunnel with a test section of 5.5 m in length, 0.8 m in width and 1.0 m in height. The freestream velocity U_∞ are measured with a Pitot-static tube, which is connected to a Furness FCO510 micro-manometer (0 - 20 mm H_2O, 0 - 18 m/s) with an uncertainty of less than 2.0%. Experiments are performed at a range of U_∞, from 6.0 - 23.4 m/s, and the corresponding longitudinal turbulence intensity is between 0.45 and 0.42% in the absence of the airfoil. Two smooth false walls of the same size with rounded leading-edge are installed near the test section inlet to ensure two-dimensional flow around the airfoil model (Fig. 1).

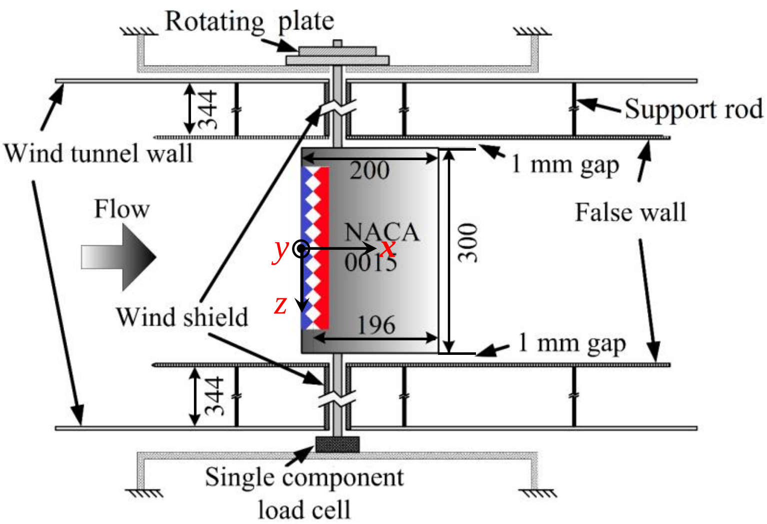

Figure 1 – Sketch of the overall experimental setup.

2.2 Airfoil Model and Plasma Actuator

A NACA 0015 airfoil with a chord length *c* of 200 mm and a spanwise length *b* of 300 mm is vertically mounted between the two false walls with 1 mm end gap, through pitching pivots (Fig. 1). The airfoil model is divided into two parts, i.e., the main airfoil body (Fig. 2a) and the airfoil hood (Fig. 2b,d). The latter, made of 1-mm thick PMMA, is used as the dielectric panel for the new sawtooth plasma actuator configuration. The airfoil hood is perfectly flush-mounted into the recess of the main airfoil body, thus forming a suction side of the airfoil. The material and the physical dimensions of the main airfoil body and the airfoil hood were identical to those used by Wang *et al*. [14]. The setting for angle-of-attack α is manually adjusted by the rotary table bolted on the overhead supporting platform, and the maximum uncertainty on α is 0.25º.

A new sawtooth plasma actuator configuration consists of two sawtooth electrodes separated by the dielectric panel, i.e., airfoil hood, and are arranged with opposite sawteeth pointing at each other. Each electrode is made of 0.15 mm thick adhesive copper foil. Note that only the upper electrode is protruded from the airfoil surface. Unlike the one (Fig. 2b) in Wang *et al*. [14] which produces the plasma discharge in the downstream direction (Fig. 2c), this new configuration (Fig. 2d) generates plasma discharge or the ionic flows in the upstream direction (Fig. 2e). The tips of the upper-sawtooth electrode point to the upstream direction and are located at 0.02c on the suction side of the airfoil, which is ahead of the separation point at $Re = 0.77 \times 10^5$ [14]. Following ref. [14], the height *h* and width *w* of the sawtooth are fixed at 17 mm and 1.5 mm, respectively. Plasma is generated toward the grounded electrode by applying a sinusoidal ac waveform to the exposed electrode with an applied voltage V_a = 15 kV at a frequency f = 11 kHz, with the grounded electrode connects to the earth. The NI LabVIEW program-controlled duty cycle (DC) and non-dimensional burst frequency $F^+ = f_b c/U_\infty$ (where f_b is the burst frequency) of the high-voltage input signal are varied from 1% to 100% (steady mode) and 0.3 to 6.0, respectively.

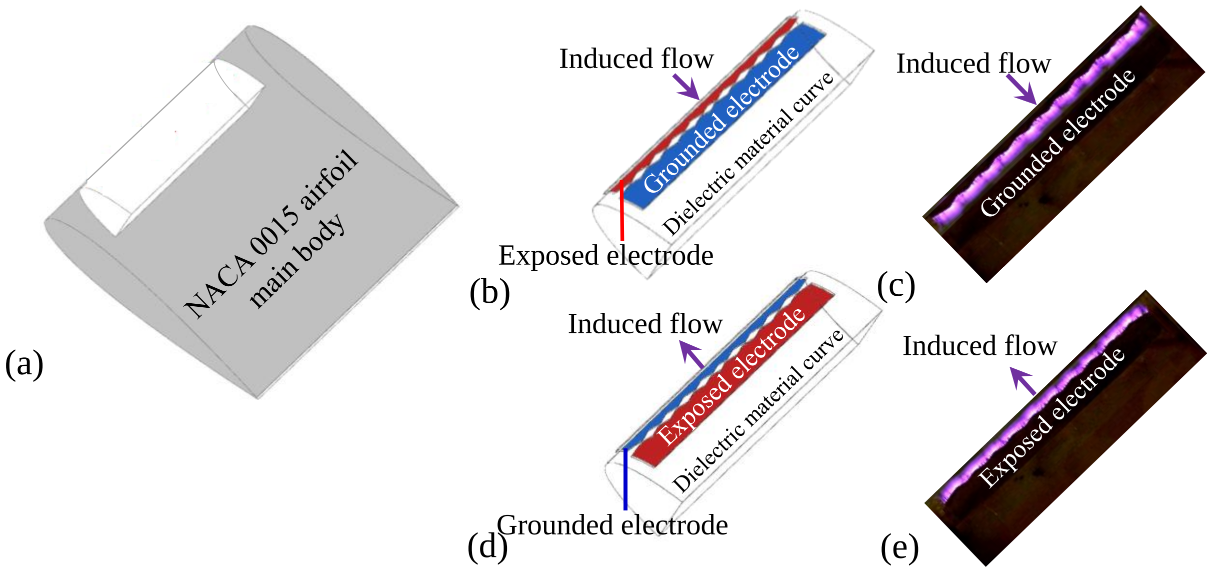

Figure 2 – (a) The main body of airfoil model, airfoil hood with downstream-directed (b) flow and (c) plasma discharge; upstream-directed (d) flow and (e) plasma discharge. The red and blue colors represent the sawtooth-shaped exposed and the grounded electrodes, respectively.

2.3 Force and Flow Visualization Measurements

The time-averaged lift force F_L is measured with a unidirectional load-cell (Interface SM-50N, S type) mounted at the bottom end of the pitching pivot (Fig. 1). The sampling rate and the sampling duration are set as 2.0 kHz and 30 seconds, respectively, for the calculation of the time-averaged F_L. The output signal of the load cell is amplified, then filtered with the cut-off frequency at 100 Hz to remove the high-frequency noise signals. The C_L (= $F_L/0.5\rho U_\infty S$, where ρ and S are the air density and the airfoil area, respectively) is achieved by normalizing F_L by the freestream dynamic pressure and the airfoil area. In all experiments, the pitching pivots and the load cell are connected to the grounded cables to release electrical charges formed by electromagnetic induction of the high-voltage cable, thus minimizing the random noise in the force measurement. In this paper, an actuator installed on the airfoil surface without plasma actuation (V_a = 0) referred as the baseline case. It is worth pointing out that due to the position of the actuator, the upper electrode may trip the boundary-layer on the suction side of the airfoil in the absence of plasma discharge at sufficiently high *Re*. As presented in Patel *et al*. [18], the sharp drop in C_L of a NACA 0015 airfoil observed at $Re \leq 2.5 \times 10^5$ relates to a laminar leading-edge stall. According to this remark, as demonstrated later in Fig. 4, the airfoil in the absence of plasma discharge undergoes laminar leading-edge stall. It is therefore the upper electrode has a negligible influence on the flow structures over the airfoil. The F_L measurements are conducted at U_∞ = 6.0 - 23.4 m/s, corresponding to the *Re* (= $\rho U_\infty c/\mu$, where μ is the dynamic viscosity of air) of 0.77×10^5 - 3.0×10^5. The standard deviation of C_L is estimated to be 1.7% based on seven-time repeated measurements. Note that force measurement is also made on the airfoil with the traditional DBD plasma actuator (hereafter called linear plasma actuator) using straight-edged exposed and grounded electrodes separated by the PMMA. This actuator is built with exactly the same size and material of the sawtooth DBD plasma.

The smoke-wire flow visualization experiments are conducted in two *x*-*y* planes (where *x* and *y* denote the streamwise and the wall-normal directions, respectively) aligned to the tip and the trough of the sawtooth electrode with and without control. U_∞ is set at 6.0 m/s in order to ensure high quality flow visualization images. A 30 mJ laser (Litron LDY304-PIV, Nd:YLF) is used in conjunction with spherical and cylindrical lenses to form a light sheet of about 1 mm thick over each *x*-*y* plane. A nichrome wire with a diameter of 0.1 mm and a length of 1360 mm is placed at 42 mm upstream of the leading edge of the airfoil, orthogonal to both airfoil span and free stream. The wire is brush painted evenly with engine oil (the viscosity of the engine oil is 1.5 Pa·s at 20℃). As the wire is heated by a 160 V dc power supply with the current of 1.6 amp, the temperature of the engine oil increases such that white smoke streamlines are generated. Images acquisition is initiated by an external trigger generated by a home-made NI program at the exact starting time of the plasma actuation. The flow images are captured above the upper surface of the airfoil at 360 frames per second with the high-speed camera (Phantom V641, and 2560 × 1600 pixel resolution) equipped with a Nikon Nikkor 90 mm lens perpendicular to the light sheet.

2.4 Particle Image Velocimetry (PIV) Measurements

A time-resolved PIV system, with the maximum trigger rate of 727 Hz for the double-frame mode, from LaVision® is used to acquire the flow field above the suction surface of the airfoil with and without plasma control. The seeding particles with diameter of 1 mm are generated by a TSI 9307-6 particles generator from Olive oil. A dual beam laser system (Litron LDY304-PIV, Nd:YLF) is used to form a light sheet of about 1 mm thick over the *x*-*y* planes for PIV measurements. The home-made NI LabVIEW program is used to generate an input signal for both high voltage power supply and PIV system, thus allowing the phase-locked measurement at different f_b and DC. The t_0 = 0s is time instant when the PA is activated. The Davis 8.3® software is used for the data acquisition and images processing. The trigger rate (sampling frequency) and sampling time are fixed at 360 Hz and 6.8 s, respectively, for the double frame mode which guarantee 20 image pairs (i.e., 20 phases) in each cycle and 120 image pairs in each phase in one measurement. It is worth pointing out that the sampling frequency is 20 times higher than the frequency of the dominant coherent structures in the separated shear layer (18 Hz). Considering that the convergence of the time-averaged behavior of the flow around the airfoil and in the unstable regions, such as the shear layer, a total of 600 image pairs are acquired from five independent series of measurements. The time between two laser pulses is set to allow one same particle moving 6 pixels between the laser pulses to increase the measurement accuracy. A high-speed CCD camera (ImagerproHS4M) equipped with Nikon Nikkor 50 mm lens perpendicular to the light sheet is used to acquire the flow field. In the image post processing, a multiple step interrogation algorithm in Davis 8.3 is used for the interrogation areas from 32 × 32 pixels^2 down to 16 × 16 pixels^2 with an overlap of 50%, and the final spatial resolution is 2.85 × 2.85 mm^2. The velocity vectors are validated using the local and median filters by calculating the deviation from the surrounding vectors. The uncertainty in the instantaneous velocity measurements outside of the shear layer is always less than 2.0%, whereas the corresponding uncertainty in the shear layer velocity measurements is estimated to be less than 6% within 95% confidence limits. As expected, the higher uncertainty is confined to the region of break-up of coherent structures at and beyond the mean reattachment point. It should be noted that the quoted values pertain to the instantaneous velocity fields, while the uncertainty in the time-averaged velocity fields is estimated to be less than 4.5%. In this paper, a superscript asterisk (*) denotes normalization by c and/or U_∞.

3. Results and Discussions

3.1 Lift Variation

Figure 3 shows the dependence of ΔC_L (= C_{Lburst} - C_{Loff}, where the subscripts burst and off denote the burst-modulated actuation and the plasma-off, respectively) on the DC and F^+ ranging from 1% to 100% (steady actuation) and 0.3 to 6.0, respectively. The α was fixed at 19º in the experiments for two reasons. Firstly, the ΔC_L is found to be the largest under the burst-modulated plasma control at Re = 0.77 × 10^5 (as demonstrated later in Fig. 4). Secondly, this α (19º) is significantly larger than the α_{stall} without plasma control at Re ranging from 0.77 × 10^5 to 3.0 × 10^5. In general, at Re = 0.77 × 10^5 - 3.0 × 10^5 the ΔC_L increases up to a certain value with increasing F^+ or DC, but declines after reaching the maximum value. At Re = 0.77 × 10^5, the maximum ΔC_L is attained at F^+ = 0.6 and DC = 5%. The optimum f_b (18 Hz) coincides with the natural vortex shedding frequency, implying that the plasma-actuated-flow interacts with the separated shear layer, causing the reattaching shear layer. Note that at DC = 5% the ΔC_L becomes small at F^+ > 3.0, possibly because the F^+ value (> 3.0) is considerably different from that of the unstable frequency of the leading-edge separated shear layer in baseline case [19].

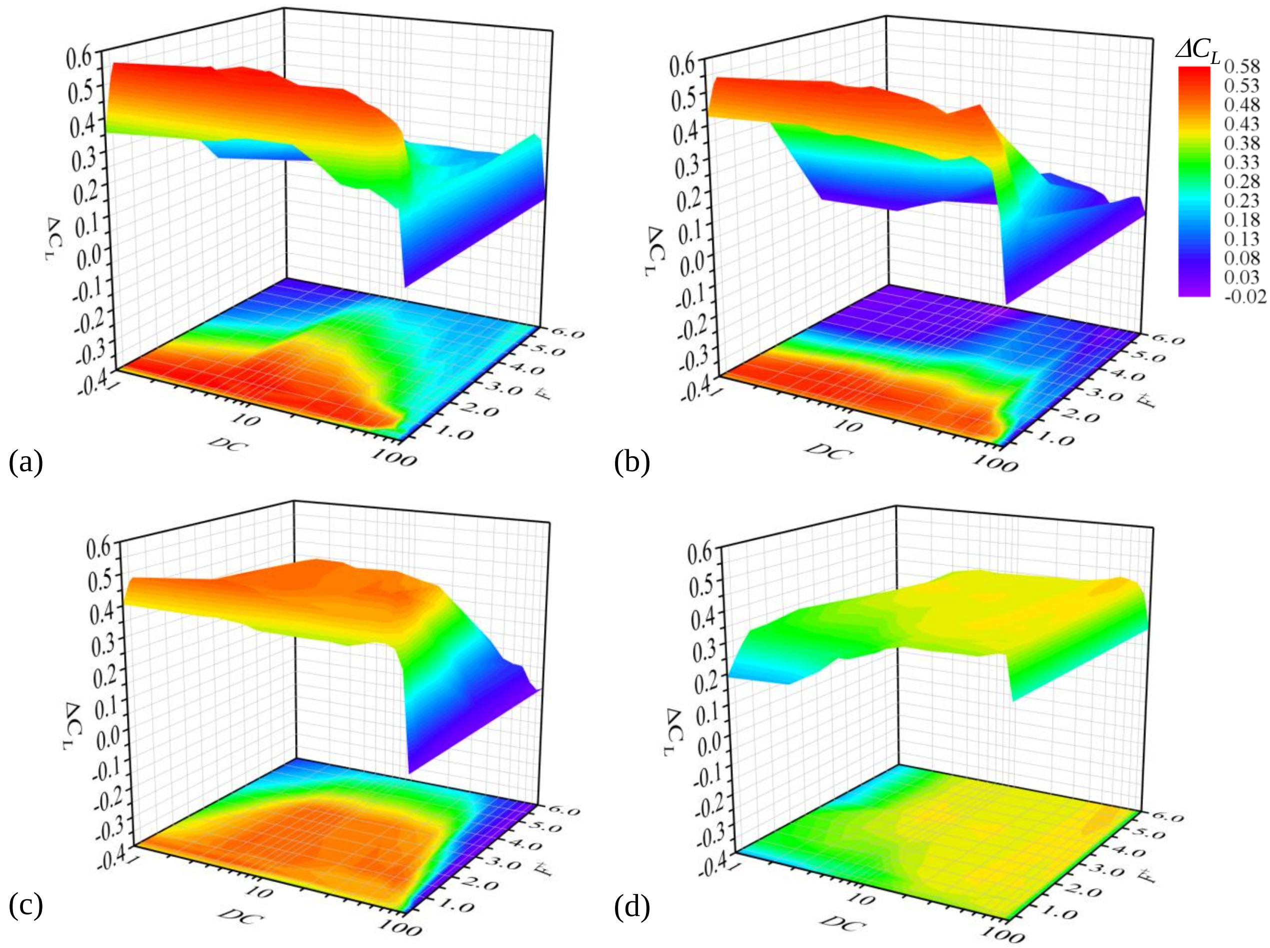

Figure 3 – Dependence of the ΔC_L on DC and F^+ at α = 19°. (a) Re = 0.77 × 10^5; (b) Re = 1.0 × 10^5; (c) Re = 2.0 × 10^5; and (d) Re = 3.0 × 10^5. V_a = 15 kV and f = 11 kHz.

At Re = 1.0 × 10^5, the maximum ΔC_L is found at DC = 10% and F^+ = 1.0 (Fig. 3b). Then, as Re increases to 2.0 × 10^5, the maximum ΔC_L is shifted to new locations at DC = 50% and F^+ = 1.5 (Fig. 3c). While, the maximum ΔC_L is located at DC = 60% and F^+ = 6.0 (Fig. 3d). People may wonder why the peak of ΔC_L disappear in Fig. 3d? In fact, the disappearance of ΔC_L peak related to the limitation to the further increase of F^+ in the present study. As reported by Sato *et al*. [20], the flow separation control with a high F^+ in the order of $O(10)$ can results in early flow reattachment effectively through the promotion of turbulent transition for Re = 2.6×10^5. The reattached flow is mainly caused by momentum entrainment into the boundary layer by fine-scale turbulent vortices. Furthermore, Sato *et al*. [21] carried out a significant parametric study to exam the effect of operating conditions of plasma actuator at $Re = 6.3 \times 10^4$. Their results showed that the effective F^+ for lift-to-drag improvement in the range of 6 to 20. Moreover, Aono *et al*. [22] investigated the effects of F^+ on the control of a deep-stall flow at $Re = 2.6 \times 10^5$. They have summarized that the optimal F^+ is higher than that at $Re = 6.3 \times 10^4$. The findings achieved by Sato *et al*. and Aono *et al*. indicate that the optimum F^+ varies with Reynolds numbers. If F^+ can be further increased to the order of 10, the prominent control performance may be achieved in further studies.

Note that the increase in DC or energy input is required to increase the strength of the plasma-induced flow structures and their interactions with the separated shear layer or vortex shedding at higher Re. At $Re = 2.0 \times 10^5$ the high-ΔC_L region (as indicated in yellowish color in Fig. 3c), covering $F^+ \approx 0.3$ - 3.6 and DC ≈ 3% - 60%, is significantly larger than its counterpart at lower $Re = 0.77 \times 10^5$ and 1.0×10^5. In particular, the positive-ΔC_L region at $Re = 3.0 \times 10^5$ (yellowish color in Fig. 3d) is largest but with minimum amplitude of increasement compared with other controlled cases (Fig. 3a-c). These finding appears reasonable considering that the coherent structures developing in the separated shear layer associated with the Kelvin–Helmholtz instability may evolve with the development of sub-harmonics and pairing [16,23], and moreover, the amalgamations of the natural vortices and the plasma-induced vortex structures may occur over the suction surface the airfoil [19]. Therefore, a wide range of F^+ is effective for increasing ΔC_L. As DC increases to 100% (steady actuation) at any given Re, the ΔC_L becomes small or negative. This is probably because the “steady” plasma-induced flow goes against or in the opposite direction to the oncoming flow, thus causing the separated shear layer to move further away from the airfoil surface.

The new sawtooth plasma actuator configuration is applied on the NACA 0015 airfoil with a view to postponing the occurrence of the stall and increasing the C_{Lmax}. Therefore, the force measurement under plasma control are made only at $\alpha \geq \alpha_{stall}$. Without plasma control, the C_L increases with α and the α_{stall} is between 14º and 16º, depending on Re. Note that the optimum values of F^+ and DC are identified and deployed in the experiments based on the largest ΔC_L in Fig. 3. Three remarkable results can be seen in Fig. 4a. Firstly, at $Re = 0.77 \times 10^5$, the C_{Lmax} achieved from the burst-modulated actuation ($F^+ = 0.6$, DC = 5% and V_a = 15 kV), including the upstream- and downstream-directed discharges of sawtooth plasma actuators, is much larger than their counterparts achieved from the steady-mode actuation. Note that in the upstream-directed discharges the burst-modulated linear plasma actuator achieves higher C_{Lmax} compared with the steady linear plasma actuator. Secondly, the burst-modulated downstream-directed discharge of sawtooth plasma actuator leads to a delay in the occurrence of αstall by 3º only and an increase in C_{Lmax} by about 27.5%. However, the burst-modulated upstream-directed discharge of the sawtooth plasma actuator manages a delay in the occurrence of αstall from 13º to 19º and an increase in C_{Lmax} by about 28.6%. Thirdly, the burst-modulated upstream-directed discharge of the linear plasma actuator only manages a delay in the occurrence of αstall from 13º to 15º and an increase in C_{Lmax} by about 22.7%; that is, under the same F^+ (0.6), DC (5%) and discharge direction, the sawtooth plasma actuator achieves better aerodynamic performance compared with the linear plasma actuator. Note that under the upstream-directed discharge control, the sawtooth plasma actuator with burst actuation produces larger C_L fluctuations compared with its counterpart with steady actuation (Fig. 5). This is because the unsteady-plasma-induced vortices aligned to the tip and tough of the sawtooth plasma actuator trigger large unsteadiness in the flow over the suction surface of the airfoil, as will be demonstrated later by the smoke-wire flow visualization images. At $Re = 1.0 \times 10^5$, $F^+ = 1.0$ and DC = 10%, the burst-modulated upstream-directed discharge may delay in the occurrence of αstall by 6º, whereas the burst-modulated downstream-directed discharge may only achieve a 2º delay in α_{stall} (Fig. 4b). At $Re = 2.0 \times 10^5$, $F^+ = 1.5$ and DC = 50%, the burst-modulated upstream-directed discharge may postpone the flow separation from the airfoil, achieving a significant rise in C_{Lmax} from 1.083 to 1.238 and delay in the occurrence of α_{stall} from

13º to 18º (Fig. 4c).

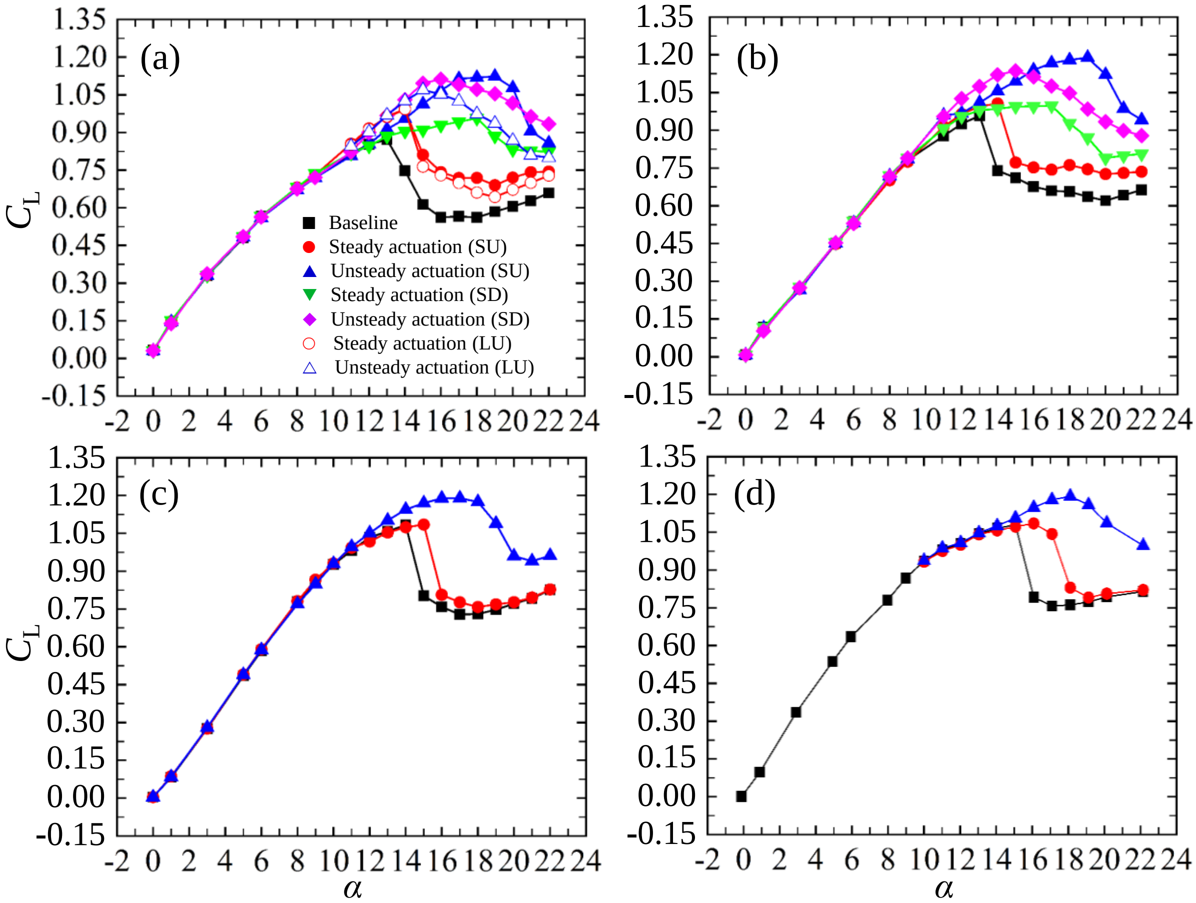

Figure 4 – Dependence of C_L on α with different actuation modes. (a) Re = 0.77 × 10^5; (b) Re = 1.0 × 10^5; (c) Re = 2.0 × 10^5; and (d) Re = 3.0 × 10^5. Linear plasma actuator (L) and sawtooth plasma actuator (S). Upstream-directed (U) and downstream-directed (D) discharge. V_a = 15 kV and f = 11 kHz.

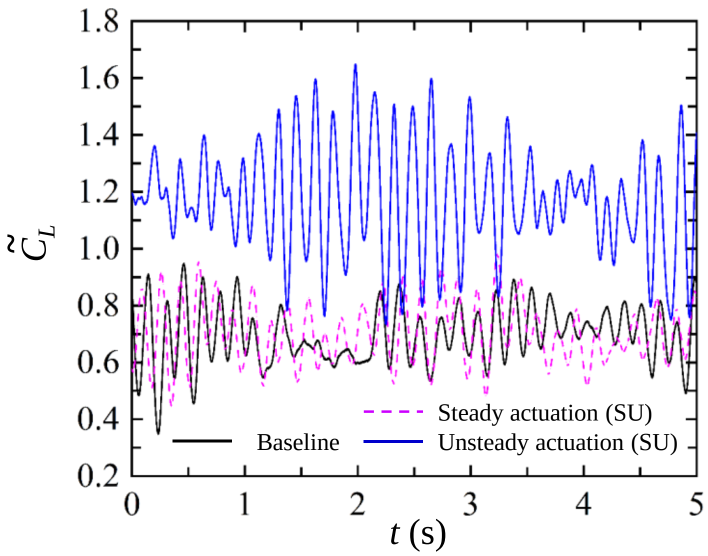

Figure 5 – Time history of instantaneous lift coefficient.

3.2 Smoke-wire Flow Visualization

Figure 6 presents the smoke-flow visualization images at α = 19º and Re = 0.77 × 10^5. Without control (Fig. 6a), the flow separates from the leading edge of the airfoil and the vortex shedding occurs over the suction surface. Likewise, with steady upstream-directed plasma control (Fig. 6b), the separation occurs at the leading edge of the airfoil, causing the airfoil to stall. The presence of the separated flow with and without steady plasma control coincides with the substantial reduction of C_L in Fig. 4a.

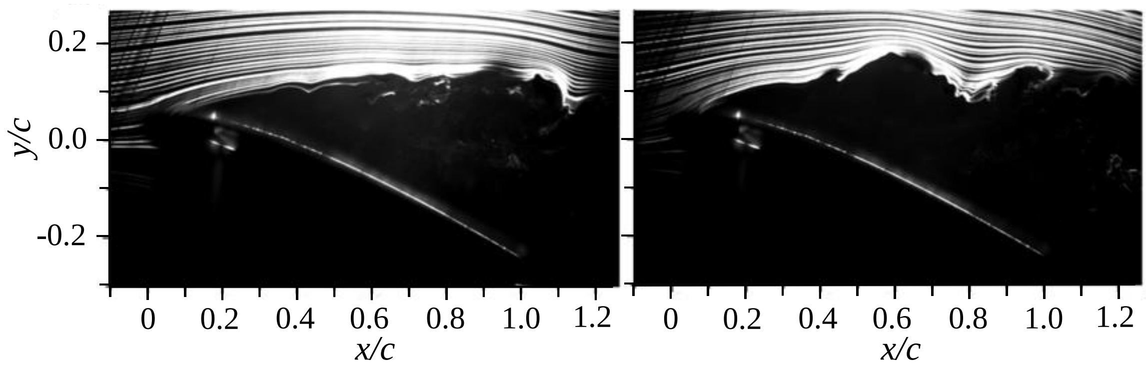

Figure 6 – Time history of instantaneous lift coefficient.

It is noteworthy that under the burst-modulated upstream-directed plasma control the image acquisition began at the exact starting time of the plasma actuation. We divide uniformly one complete actuation cycle (2π) into 20 phases with a constant phase angle φ shift of π/10. The phase (at φ = 0) of initial discharge and several phases (at φ = 3π/10, 7π/10, π, 14π/10 and 19π/10) after the initial discharge are displayed in Figs. 7 and 8 to demonstrate the flow structures and their movements that are predominantly responsible for the enhanced aerodynamic performance. At F^+ = 0.6, DC = 5% and V_a = 15 kV, and on the visualization plane aligned to the tip of the sawtooth DBD plasma actuator (Fig. 7), the initial discharge in the upstream direction (Fig. 2e) generates the upstream-directed jet as a result of the momentum transfer from the discharge to the fluid. This upstream-directed jet interacts locally with the freestream flow, and subsequently, forms a resultant flow which is in the downstream direction and above the suction surface of the airfoil. This resultant flow tends to roll-up, due to the acceleration within the upstream-directed surface-plasma-discharge region, forming a large-scale vortex which displays as a dark region in the image at φ = 3π/10. This vortex is highlighted in a red circle with arrows indicating the clockwise rotation in Fig. 7b.

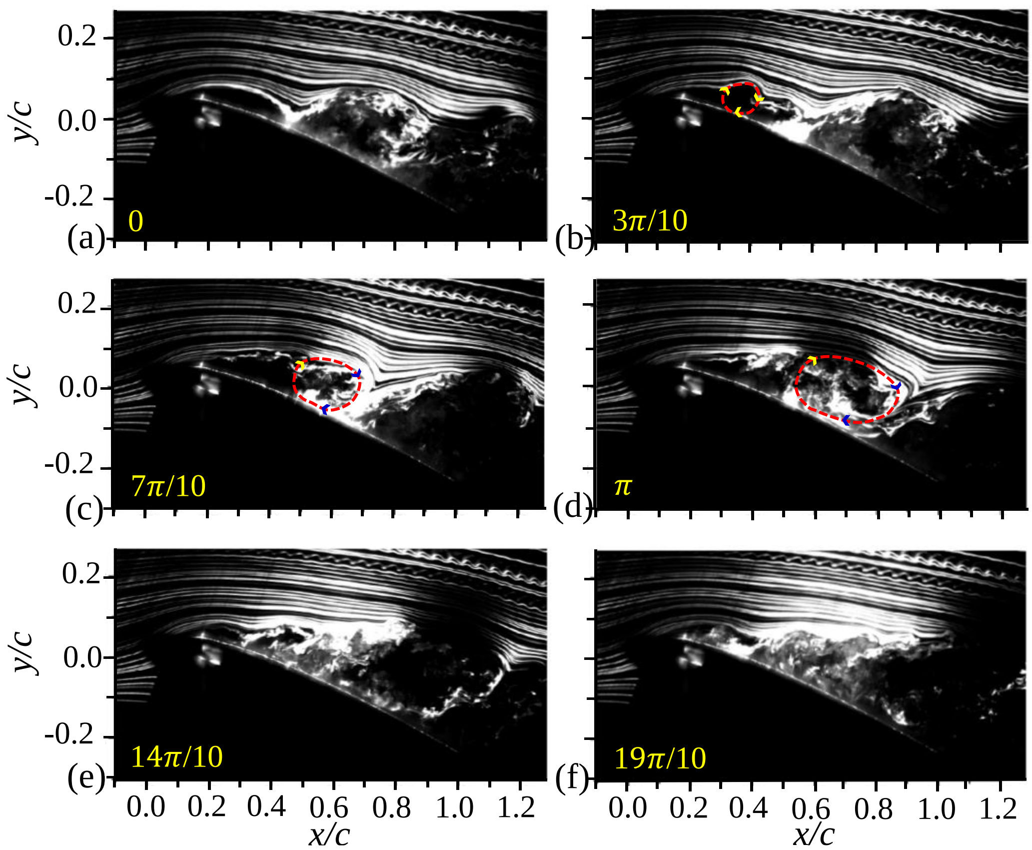

Figure 7 – Smoke-wire flow visualization aligned to the tip of the sawtooth: burst-modulated actuation (F^+ = 0.6, DC = 5%, V_a = 15 kV, and $Re = 0.77 \times 10^5$).

Note that this large-scale vortex occurs at approximately $x = 0.2c$ - $0.4c$ over the suction side of the airfoil and is advected downstream, pushing the reattachment point toward $x = 0.6c$ as shown at $\varphi = 7\pi/10$ (Fig. 7c). This large-scale vortex evolves and diffuses as shown at $\varphi = \pi$ and $14\pi/10$ (Figs. 7d-e), causing the instability of the separated shear layer over the entire suction side of the airfoil as shown at $\varphi = 19\pi/10$ (Fig. 7f). The generation of the large-scale vortex at the leading edge of the airfoil and its development and evolution over the suction surface is expected to enhance the C_L and to delay the αstall. On the contrary, under the same V_a and DC, but at $F^+ = 6.0$, the large-scale vortex could not be generated at the leading edge of the airfoil (not shown), and as a result, the separated shear layer fails to reattach on the airfoil upper surface and the airfoil is stalled.

It is noteworthy that the discharge filaments emerging from the adjoining edges and near the trough of the upper electrode bend toward the grounded electrode in opposite directions [11]. However, the generation of the near-wall vortices is unlikely to occur at the trough region of the sawtooth. This is because the plasma-induced curled-flow at the trough region of the sawtooth is overwhelmed by the relatively high-velocity freestream flow. Despite the foregoing expectation, the flow in the visualization plane aligned to the trough of the sawtooth DBD plasma actuator (Fig. 8) is different from that aligned to the tip of the sawtooth (Fig. 7). At $F^+ = 0.6$, DC = 5% and $V_a = 15$ kV, the initial discharge at the trough of the sawtooth generates the upstream-directed flow and interacts locally with the freestream flow. Similar to that aligned to the tip of the sawtooth, a resultant flow is generated in the downstream direction, but apparently closer to the airfoil surface (Fig. 8a). This resultant flow rolls up and forms a relatively smaller-scale vortex which takes place as a dark region between $0.25c$ and 0.4c (Fig. 8b). The vortex evolves over the suction surface of the airfoil as shown at $\varphi = 7\pi/10$ and π, pushing the reattachment point toward $x = 0.7c$ and $0.8c$, respectively (Figs. 8c, d). The vortex diffuses as shown at $\varphi = 14\pi/10$ and $19\pi/10$, resulting in a large region of reattaching flow covering the entire suction surface (Figs. 8e, f).

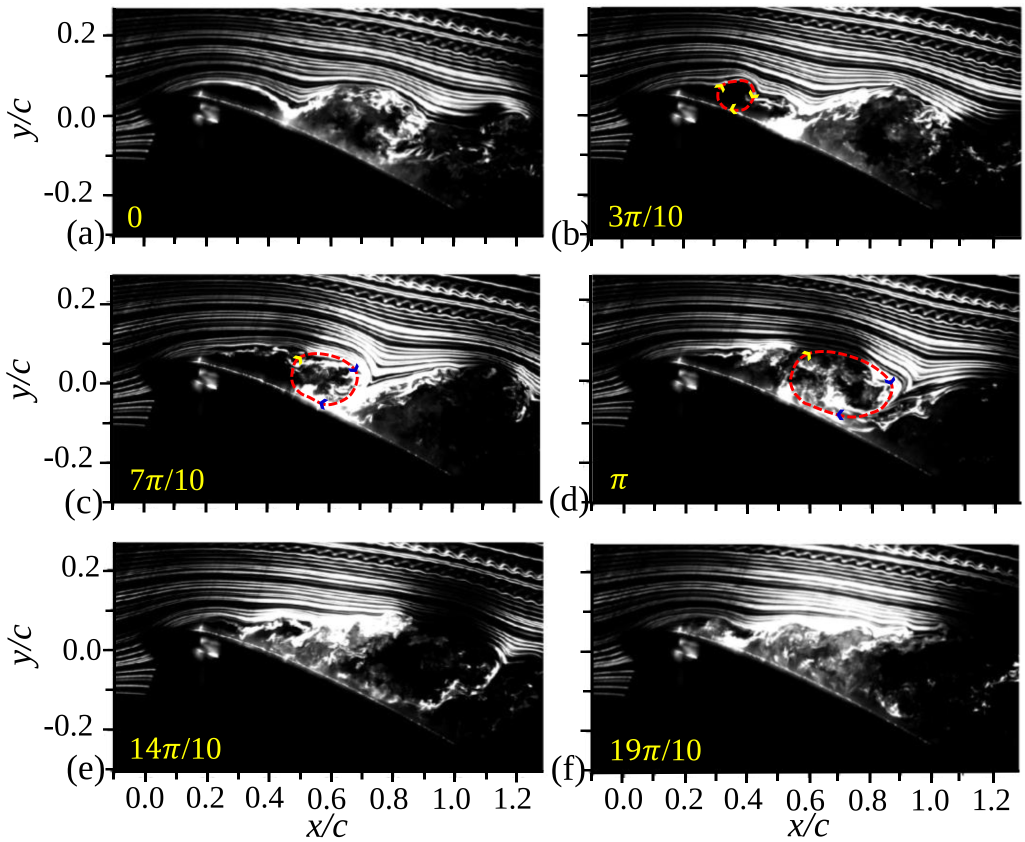

Figure 8 – Smoke-wire flow visualization aligned to the trough of the sawtooth: burst-modulated actuation ($F^+ = 0.6$, DC = 5%, $V_a = 15$ kV, and $Re = 0.77 \times 10^5$).

One scenario is proposed for the enhanced C_L. The new sawtooth plasma actuator configuration generates the upstream-directed plasma discharges or ionic flows along the sawtooth-edge of the upper electrode. The plasma-induced flow velocity would vary along the sawtooth electrode edge [11]. There exists a noticeable increase of plasma density at the tip compared to the trough region of the sawtooth (Fig. 2e), indicating that the flow velocity at the tip of the sawtooth is higher than that at the trough of the sawtooth. These upstream-directed flows interact and overwhelmed by the oncoming flow, forming the resultant flows that are in the downstream direction and above the suction surface of the airfoil. The foregoing observation explicitly demonstrates that the velocity magnitude of the resultant flows is varied periodically in the *z*-direction. These resultant flows are dragged by the acceleration within the upstream-directed plasma-discharge region, and as a result, different scales of spanwise vortices are formed in the *x*-*y* planes that are aligned to the tip and the trough of the sawtooth electrode (Figs. 7 and 8). It is noted that at $\varphi = 3\pi/10$ the spanwise vortex aligned to the tip of the sawtooth is approximately two times larger (measures from the core to the edge of the vortex) than that aligned to the trough of the sawtooth. Nevertheless, the trajectory of these spanwise-alternating large- and small- scale vortices follow closely to the upper surface, advecting from the leading-edge to the trailing-edge of the airfoil, causing the rapid rise in the suction pressure on the upper surface. Therefore, “additional” lift force is generated on the airfoil.

3.3 Flow Fields

Figure 9 shows the non-dimensional time-averaged streamwise velocity $\bar{u}^*$ in the cases of baseline and steady plasma actuation in P-P plane at *Re* = 0.77 × 10^5. The modified fields of $\bar{u}^*$ in T-T plane are almost same with those in P-P plane, and the figure not shown here. In the baseline case, flow separation appears at the leading edge of airfoil and the large recirculation region resist above the suction surface of airfoil (Fig. 9a). Due to the effect of forward flow induced by sawtooth plasma actuator under steady mode, the shear layer at the leading edge of airfoil forced to separate from suction surface earlier by the stronger adverse pressure gradient (Fig. 9b). This is clearly shown by the curved streamline which flow above the leading edge and moves downstream.

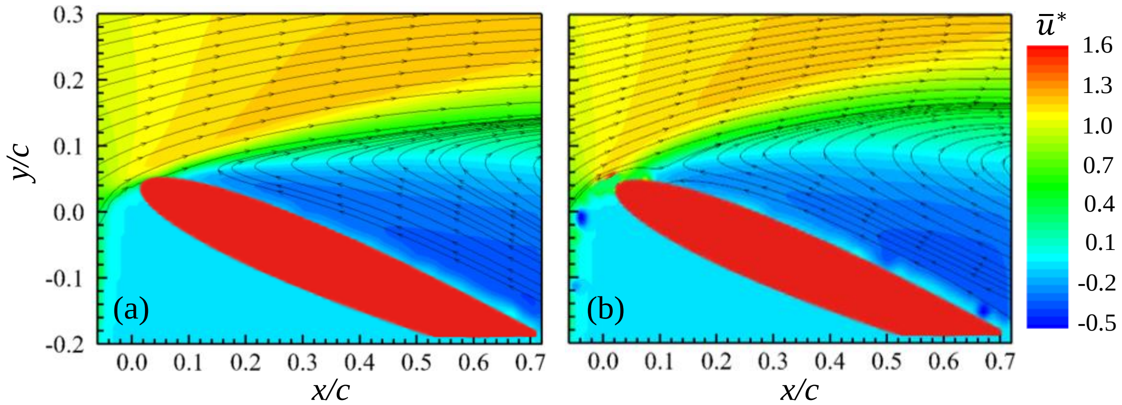

Figure 9 – The non-dimensional time-averaged streamwise velocity $\bar{u}^*$ (= $\bar{u}/U_\infty$) with streamlines. (a) Baseline and (b) steady plasma actuation in P-P plane.

In general, there exist some interactions of the periodic disturbances near the suction surface (Fig. 10); for instance, the periodic disturbances may lead to intense turbulent flow fluctuations that attach on the surface. At $\varphi = 0$, the plasma actuation generates disturbance which emerges aft of the sawtooth electrode (anode). It should be noted here the large-scale recirculation region above suction surface of airfoil at $\varphi = 0$ and $\pi/10$ induced by plasma actuation form previous cycle. From $\varphi = 3\pi/10$, the disturbance generated at $\varphi = 0$ results in a reattachment bubble at the leading edge. At $\varphi = 3\pi/10$ - $5\pi/10$, the disturbance develops into turbulent flows that propagate downstream of the actuator. Meanwhile, the flow attachment region extends up from 0.18*c* at $\varphi = 3\pi/10$ to 0.26*c* at $\varphi = 5\pi/10$. At $\varphi = 5\pi/10$, due to the decay of the forcing and the increase of advance pressure gradient near the trailing edge, the reattached flow from the previous plasma actuation cycle leaving from the suction surface and totally disappear at $\varphi = 11\pi/10$. From $\varphi = 11\pi/10$, there is only one attached vortex flow on the suction surface and moves downstream gradually. The reattachment point moves from 0.4*c* at $\varphi = 14\pi/10$ to 0.65*c* at $\varphi = 19\pi/10$ and disappear in the next plasma actuation cycle. As illustrated in the flow visualizations (Fig. 7), one attached vortex flow can be induced in each actuation cycle. These vortices advect from the leading-edge to the trailing-edge of the airfoil, causing the rise in the suction pressure. Therefore, the C_L is substantially increased.

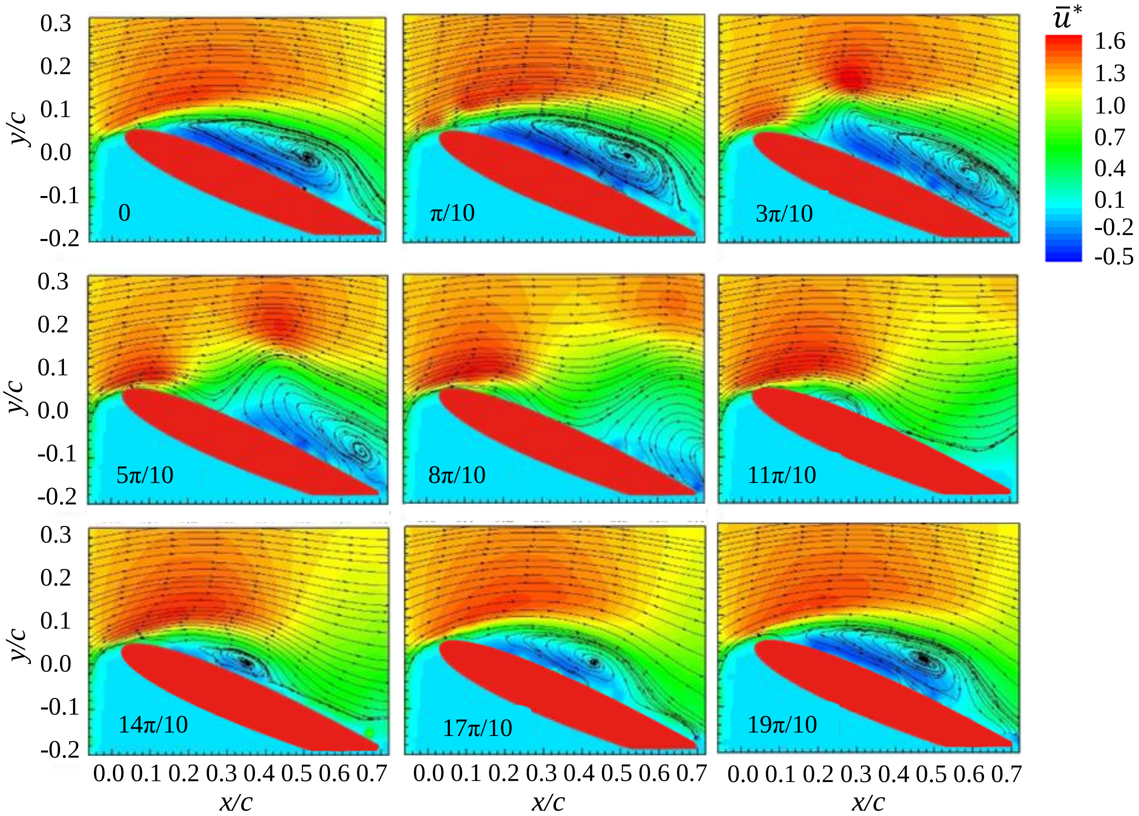

Figure 9 – The non-dimensional Phase-averaged streamwise velocity $\bar{u}^*$ (= $\bar{u}/U_\infty$) with streamlines. in P-P plane under unsteady plasma actuation. (F^+ = 0.6, DC = 5%).

4. Conclusions

Experimental investigation is performed to suppress flow separation from a NACA 0015 airfoil using a new sawtooth DBD plasma actuator configuration at *Re* ranging from 0.77 × 10^5 to 3.0 × 10^5. The new sawtooth plasma actuator configuration generates the upstream-directed plasma discharge or the ionic flows that oppose the oncoming flow. The C_L is measured over 380 combinations of F^+ and DC levels at four *Re* (0.77 × 10^5, 1.0 × 10^5, 2.0 × 10^5 and 3.0 × 10^5). As a result, the optimum F^+ and DC are identified where the highest C_L is achieved for each *Re*. The following conclusions can be drawn.

(1) Under burst-modulated operation at F^+ = 0.6 and DC = 5% for *Re* = 0.77 × 10^5, this new sawtooth DBD plasma actuator configuration, which produces the upstream-directed plasma discharge, manages a delay in the occurrence of α_{stall} from 13º to 19º and an increase in C_{Lmax} by about 28.6%, whereas the downstream-directed plasma discharge achieves a delay in the occurrence of α_{stall} from 13º to 16º and an increase in C_{Lmax} by about 27.5%. The C_{Lmax} is found to be similar in these two cases, perhaps due to the small difference in the strength of the upstream- and downstream- plasma induced spanwise vorticity over the airfoil surface. On the other hand, it is evident that under the same V_a the new actuator configuration operated in burst-modulated mode achieves an α_{stall} of 19º and a C_{Lmax} of 1.123, which are larger than 14º and 0.992, respectively, achieved by the same actuator configuration operated in steady mode. It has been found that at F^+ = 0.6, DC = 5% and V_a = 15 kV, the linear plasma actuator with the burst-modulated upstream-directed discharge only manages a delay in the occurrence of α_{stall} from 13º to 15º and an increase in C_{Lmax} by about 22.7%; that is, the sawtooth plasma actuator achieves larger α_{stall} and C_{Lmax} compared with the linear plasma actuator under the same F^+, DC and V_a.

(2) Physical mechanisms behind the improved control performance have been studied. The initial discharges along the sawtooth electrode edge generate the upstream-directed flows. The flow velocity at the tip of the sawtooth is larger than that in the trough region of the sawooth as a result of the intense discharge density occurring at the tip of the sawooth electrode. The flows induced by this sawtooth plasma actuator interact locally with the freestream flow, and as a result, form the

resultant flows that are in the downstream direction. In fact, these resultant flows tend to roll-up, forming the large-scale vortex aligned to the tip of the sawtooth or the small-scale vortex aligned to the trough of the sawtooth as observed in the smoke-flow visualization images. The trajectory of these spanwise-alternating large- and small- scale vortices is found to follow closely to the upper surface. They advect from the leading-edge to the trailing-edge of the airfoil, causing the rise in the suction pressure. Therefore, the C_L is substantially increased.

5. Acknowledgement

Authors wish to acknowledge support by the National Natural Science Foundation of China through grant 11502060 and 12002110 and from the Research Grants Council of the Shenzhen Government through grants JCYJ20160531193045101 and GXWD20201230155427003-20200824094301001.

6. Copyright Statement

References

[1] Lissaman P B S. Low-Reynolds-number airfoils. *Annual Review of Fluid Mechanics*, Vol. 15, No. 1, pp 223-239, 1983.

[2] Post M L and Corke T C, Separation control on high angle of attack airfoil using plasma actuators. *AIAA Journal*, Vol. 42, No. 11, pp 2177-2184, 2004.

[3] Patel M P, Ng T T, Vasudevan S, Corke T C, Post M L, McLaughlin T E and Suchomel C F. Scaling effects of an aerodynamic plasma actuator. *Journal of Aircraft*, Vol. 45, No. 1, pp 223-236, 2008.

[4] Kelley C L, Bowles P O, Cooney J, He C, Corke T C, Osborne B A, Silkey J S and Zehnle J. Leading-edge separation control using alternating-current and nanosecond-pulse plasma actuators. *AIAA Journal*, Vol. 52, pp 1871–84, 2014.

[5] Wang J J, Choi K S, Feng L H, Jukes T N and Whally R D. Recent developments in DBD plasma flow control. *Progress in Aerospace Sciences*, Vol. 62, No. 4, pp 52-78, 2013.

[6] Konstantinidis E. Active control of bluff-body flows using plasma actuators. *Actuators*, Vol. 8, No. 3, pp 1-28, 2019.

[7] Forte M, Jolibois J, Pons J, Moreau E, Touchard G and Cazalens M, Optimization of a dielectric barrier discharge actuator by stationary and non-stationary measurements of the induced flow velocity: application to airflow control. *Experiments in Fluids*, Vol. 43, No. 6, pp 917-928, 2007.

[8] Enloe C L, McLaughlin T E, VanDyken R D, Kachner K D, Jumper E J and Corke T C. Mechanisms and responses of a single dielectric barrier plasma actuator: geometric effects. *AIAA Journal*, Vol. 42, No. 3, pp 595-604, 2004.

[9] Benard N, Mizuno A and Moreau E. A large-scale multiple dielectric barrier discharge actuator based on an innovative three-electrode design. *Journal of Physics D: Applied Physics*, Vol. 42, No. 23, 2009.

[10] Durscher R J and Roy S. Three-dimensional flow measurements induced from serpentine plasma actuators in quiescent air. *Journal of Physics D: Applied Physics*, Vol. 45, No. 3, 2012.

[11] Joussot R, Leroy A, Weber R, Rabat H, Loyer S and Hong D. Plasma morphology and induced airflow characterization of a DBD actuator with serrated electrode. *Journal of Physics D: Applied Physics*, Vol. 46, No. 12, 2013.

[12] Wong C W, Wang L J, Wu Z, Li C H, Alam M M and Zhou Y. Control of separated flow on a NACA 0015 airfoil using three-dimensional plasma actuator. 7th AIAA Flow Control Conference, Atlanta, GA, USA, Paper No. 2014-2665, June 2014.

[13] Lu Z Y, Wong C W, Wang L J, Alam M M and Zhou Y. Separation control on a NACA 0015 airfoil with plasma-actuator-generated disturbance. 8th AIAA Flow Control Conference, Washington, D.C. USA, Paper No. 2016-3625, June 2016.

[14] Wang L J, Wong C W, Lu Z Y, Wu Z and Zhou Y. Novel sawtooth dielectric barrier discharge plasma actuator for flow separation control. *AIAA Journal*, Vol. 55, No. 4, pp 1405-1416, 2017.

[15] Wang L J, Wong C W, Fu X D and Zhou Y. Influence of burst-modulated frequency on sawtooth DBD plasma actuator for flow separation control. 2018 AIAA Aerospace Sciences Meeting, Kissimmee, Florida, USA, Paper No. 2018-1062, Jan. 2018.

[16] Wang L J, Wong C W, Alam M M and Zhou Y. Post-stall flow control using a sawtooth plasma actuator in burst mode. *Aerospace Science and Technology*, Vol. 107, pp 1-18, 2020.

[17] Zhang X, Li H X, Huang Y and Wang W B. Wing flow separation control using asymmetrical and symmetrical plasma actuator. *Journal of Aircraft*, Vol. 54, No. 1, pp 301-309, 2016.

[18] Patel M P, Sowle Z H, Corke T C and He C. Autonomous sensing and control of wing stall using a smart plasma slat. *Journal of Aircraft*, Vol. 44, pp 516-527, 2007.

[19] Aono H, Kawai S, Nonomura T, Sato M, Fujii K and Okada K. Plasma-Actuator burst-mode frequency effects on leading-edge flow-separation control at Reynolds number 2.6×10^5. *AIAA Journal*, Vol. 55, pp 3789-3806, 2017.

[20] Sato M, Okada K, Asada K, Aono H, Nonomura T and Fujii K. Unified mechanisms for separation control around airfoil using plasma actuator with burst actuation over Reynolds number range of 10^3–10^6. Physics of Fluids, Vol. 32, pp 1-27, 2020.

[21] Sato M, Aono H, Yakeno A, Nonomura T, Fujii K, Okada K and Asada K. Multifactorial effects of operating conditions of dielectric-barrier-discharge plasma actuator on laminar-separated-flow control. *AIAA Journal*. Vol 53, pp 2544-2559, 2015.

[22] Aono H, Kawai S, Nonomura T, Sato M, Fujii K and Okada K. Plasma-actuator burst-mode frequency effects on leading-edge flow-separation control at Reynolds number 2.6×10^5. *AIAA Journal*. Vol. 55, pp 3789-3806, 2017.

[23] Yarusevych S, Sullivan P E and Kawall J G. On vortex shedding from an airfoil in low-Reynolds-number flows. *Journal of Fluid Mechanics*, Vol. 632, pp 245-271, 2009.